Title

Motion robust high resolution 3D free-breathing pulmonary MRI using dynamic 3D image self-navigator

Journal

Magnetic Resonance in Medicine, 79(6)

ISSN

0740-3194

Authors

Jiang, Wenwen
Ong, Frank
Johnson, Kevin M
et al.

Publication Date

2018-06-01

DOI

10.1002/mrm.26958

Peer reviewed

HHS Public Access

Author manuscript

Magn Reson Med. Author manuscript; available in PMC 2019 June 01.

Published in final edited form as:

Magn Reson Med. 2018 June ; 79(6): 2954–2967. doi:10.1002/mrm.26958.

Motion Robust High Resolution 3D Free-Breathing Pulmonary MRI Using Dynamic 3D Image Self-Navigator

Wenwen Jiang[1], **Frank Ong**[2], **Kevin M. Johnson**[3,4], **Scott K. Nagle**[3,4], **Thomas A. Hope**[5], **Michael Lustig**[1,2], and **Peder E.Z. Larson**[1,5,*]

[1]UC Berkeley-UCSF Graduate Program in Bioengineering, University of California, Berkeley and University of California, San Francisco, California, USA.

[2]Department of Electrical Engineering and Computer Sciences, University of California, Berkeley, California, USA.

[3]Department of Medical Physics, University of Wisconsin, Madison, Madison, Wisconsin, USA.

[4]Department of Radiology, University of Wisconsin, Madison, Madison, Wisconsin, USA.

[5]Department of Radiology and Biomedical Imaging, University of California, San Francisco, California, USA.

Abstract

Purpose: To achieve motion robust high resolution 3D free-breathing pulmonary MRI utilizing a novel dynamic 3D image navigator derived directly from imaging data.

Methods: Five-minute free-breathing scans were acquired with a 3D ultrashort echo time (UTE) sequence with 1.25 mm isotropic resolution. From this data, dynamic 3D self-navigating images were reconstructed under locally low rank (LLR) constraints and used for motion compensation with one of two methods: a soft-gating technique to penalize the respiratory motion induced data inconsistency, and a respiratory motion-resolved technique to provide images of all respiratory motion states.

Results: Respiratory motion estimation derived from the proposed dynamic 3D self-navigator of 7.5 mm isotropic reconstruction resolution and a temporal resolution of 300 ms was successful for estimating complex respiratory motion patterns. This estimation improved image quality compared to respiratory belt and DC-based navigators. Respiratory motion compensation with soft-gating and respiratory motion-resolved techniques provided good image quality from highly undersampled data in volunteers and clinical patients.

Conclusion: An optimized 3D UTE sequence combined with the proposed reconstruction methods can provide high-resolution motion robust pulmonary MRI. Feasibility was shown in

*Correspondence to: Peder E.Z. Larson, Ph.D., Suite 102, Byers Hall, University of California, San Francisco, San Francisco, CA 94158. peder.larson@ucsf.edu; Twitter: @pezlarson.

Presented in part at the 24th Annual Meeting of ISMRM, Singapore, 2016. Received 24 February 2017; revised 16 August 2017; accepted 14 September 2017 DOI 10.1002/mrm.26958

SUPPORTING INFORMATION

Additional Supporting Information may be found in the online version of this article.

patients who had irregular breathing patterns in which our approach could depict clinically relevant pulmonary pathologies.

Keywords

3D self-navigator; UTE; free-breathing; soft-gating; respiratory motion-resolved; pulmonary imaging

INTRODUCTION

Pulmonary imaging with MRI has potential to characterize soft tissue using the wide range of available image contrasts (e.g., T_1, T_2, diffusion, perfusion, and ventilation). Further, the use of MRI in place of CT avoids radiation dose which carries substantial risks with repeated radiation exposure (1–4). These benefits of pulmonary MRI are most relevant in pediatric diseases requiring longitudinal follow-up, such as cystic fibrosis (CF) and assessing pulmonary nodules, and can also enable imaging studies in much more widespread lung diseases such as asthma. However, achieving morphological lung MRI with comparable diagnostic value to CT is challenging due to the combined factors of short T_2^*, low proton density, and respiratory motion.

A variety of pulse sequence techniques and acquisition procedures have been developed to address these challenges (5–12). Among these techniques, radial ultrashort echo time (UTE) imaging has shown significant promise for high-quality pulmonary imaging due to its ability to capture the rapidly decaying signal and its robustness to motion (5,11,12). Recently, 3D radial UTE sequences with readout optimized for SNR efficiency have been proposed (12) for free-breathing pulmonary imaging. They have shown the potential to provide comparable image quality to CT in several recent studies (13,14). While these techniques enable the assessment of lung parenchyma, they remain reliant on effective motion compensation which can be challenging in the populations in which they are most needed (e.g., pediatrics).

For a respiratory motion compensation model to be effective, accurate motion estimation must first be obtained. External respiratory bellows can be used to estimate respiratory motion but are prone to errors. Most dominantly, the motion of the abdominal wall is often poorly coupled to actual lung motion which leads to inaccurate respiratory motion estimation (12,15). Motion information can be alternatively extracted directly from the acquired k-space data as a self-navigator. A common approach is to use the k-space center (DC), representing the average signal of the excitation volume, as a self-navigation signal (15–25). Image-based self-navigation can provide a direct measurement of motion, and recent studies have shown that this approach had significantly better image sharpness than any of the DC-based self-navigation methods (26,27).

To account for respiratory motion when reconstructing images, a variety of methods have been proposed. One class of methods aims to explicitly solve for motion displacement and compensate it during the reconstruction. In particular, Batchelor and others (28–30) proposed generalized matrix models to incorporate arbitrary motion displacement operators into the forward reconstruction model. Methods using image registration (31–39) were also

proposed to correct for motion by iteratively alternating between image registration and reconstruction. Additionally, Cheng and others proposed local auto-focusing methods (21,40–43) to choose the sharpest image in a local region according to a gradient entropy metric. While these methods were shown to be effective to reduce motion artifacts in many applications, errors in their underlying motion models may introduce artifacts.

For this work, we focus on another class of reconstruction methods that implicitly exploits image correlations from different respiratory motion states. While compromising the ability to correct for motion, this class of methods is very robust to motion model errors. In particular, we focused on soft-gating (44–47) and motion-resolved methods (48). Soft-gating is a computationally efficient iterative method in which the data consistency term in the optimization is preferentially weighted based on distances from the chosen respiratory motion state. The motion-resolved method, on the other hand, divides the data into several respiratory motion states and enforces correlations between motion states in an iterative reconstruction.

The purpose of this work is to provide motion robust high resolution 3D pulmonary imaging using the following approach: I. Data acquisition with an optimized 3D UTE sequence, II. Motion estimation with a lower-resolution, high frame rate dynamic 3D self-navigator from the subset of acquired data with reconstruction that combines parallel imaging (49) and compressed sensing (50) with locally low-rank constraints (51,52), III. Motion compensation using a retrospective soft-gating technique to reconstruct high-resolution images at a chosen motion state, IV. A respiratory motion-resolved technique to provide images of all respiratory motion states, and V. The incorporation of L1-ESPIRiT (53), an auto-calibrating parallel imaging and compressed sensing method. The proposed methods are based on a 5-min free-breathing scan, which is comparable to other free-breathing pulmonary MRI sequences (14,39,54). We applied the proposed methods on healthy volunteers as well as subjects with CF and pulmonary nodules to demonstrate feasibility for clinical applications.

METHODS

Data Acquisition

An optimized free-breathing 3D radial UTE sequence with slab excitation and a bit-reversed view ordering from Johnson et al. (12) was implemented. It incorporates variable density readout gradients to improve SNR efficiency and slab excitation to reduce the number of encodings and artifacts from the fringe of the gradient and B_0 fields. The pseudorandom view ordering determined by a bit-reversed algorithm mitigates structured artifacts enabling free-breathing pulmonary imaging. Specific acquisition parameters are described in the following Experiment section.

Based on this sequence, the acquired data is reconstructed in a two-step process illustrated in Figure 1. First, high frame rate, lower-resolution dynamic 3D images are reconstructed for self-navigation, followed by respiratory motion estimation. Second, these estimates are used for a motion compensated high resolution reconstruction using soft-gating L1-ESPIRiT or respiratory motion-resolved L1-ESPIRiT reconstructions described below.

Respiratory Motion Estimation

In radial acquisitions, the center of k-space is sampled repeatedly, which can be exploited for motion estimation. Changes in the k-space center (DC) signal reflect changes in average image intensity and phase that can be used for motion estimation, and multiple coils can further provide localized information (18,55–58). However, DC signals are susceptible to signal intensity drifts that could arise from scanner instability by gradient induced heating (59,60), and also remain sensitive to bulk motion or the rotating of readout direction. Thus, they often lack direct correspondence with respiratory motion. In addition, DC signals are non-quantitative and only represent the shape and intensity of the motion qualitatively. Motivated by these limitations, we propose a novel image-based self-navigated method using lower-resolution dynamic 3D images to quantitatively estimate respiratory motion.

Dynamic 3D Self-Navigator Using Locally Low-Rank Constraints

Here we describe a new method to reconstruct high frame rate, lower-resolution dynamic 3D images from the radial UTE central k-space data for motion estimation by exploiting both parallel imaging and spatiotemporal correlations with locally low-rank constraints. The 3D UTE acquisition uses a pseudo-random view ordering such that every subset of contiguously acquired radial profiles covers k-space with a relatively uniform angular distribution, which enables resolving lower-resolution dynamic images. However, to achieve sufficient temporal resolution (≥ 2 Hz) and acceptable spatial resolution (≤ 1 cm) to visualize respiratory motion, it requires more than 200-fold undersampling for every frame with respect to the Nyquist criterion for radial sampling. This is far beyond the maximum undersampling factor of typical parallel imaging and spatially constrained compressed sensing methods. Therefore, we propose to iteratively solve for lower-resolution navigation images from consecutive subsets of data by exploiting spatiotemporal correlations with locally low-rank (LLR) (51,52) constraints. These constraints provide additional prior information in order to better resolve aliased lower-resolution images. We formulate the problem in a parallel imaging and compressed sensing manner shown in Equation [1]:

$$\underset{M_{\mathrm{lr}}}{\operatorname{argmin}} \frac{1}{2}\|DSM_{\mathrm{lr}} - y_{\mathrm{lr}}\|_2^2 + \lambda \sum_{i \in \Omega} \|L_i M_{\mathrm{lr}}\|_* \quad (1)$$

Here, the first term enforces data consistency in which M_{lr} represents dynamic lower-resolution images (3D spatial + 1D temporal size: $n_x \times n_y \times n_z \times n_t$), y_{lr} are acquired multi-channel data from the central region of radial k-space measurements, S represents the sensitivity map operator (which can be estimated by ESPIRiT), and D is the multi-channel non-uniform Fourier Transform (3D radial) operator. The second term enforces LLR constraint, in which the dynamic images M_{lr} can be partitioned into a set Ω of small image blocks (size: $b_x \times b_y \times b_z \times n_t$), L_i is the operator that takes the block i of the image to form its Casorati matrix with an appropriate block size, and λ is a weighting factor to balance the constraints. This optimization problem in Equation [1] was solved by a fast iterative shrinkage-thresholding algorithm (FISTA) (61) with singular value thresholding and randomized block shifting (62).

Motion Compensated Reconstruction

At their core, our motion compensated reconstructions use parallel imaging and compressed sensing to exploit the coil sensitivities and image transform sparsity for recovering both unacquired and corrupted k-space samples. This enables a clinically-feasible 5-min scan, which typically has more than 8-fold undersampling with respect to the Nyquist criterion when motion is ignored. We propose two motion compensation strategies, soft-gating and respiratory motion-resolved, and incorporate them into an L1-ESPIRiT reconstruction framework.

General Reconstruction Framework - L1-ESPIRiT

We use L1-ESPIRiT, a combined parallel imaging and compressed sensing approach, as the basic reconstruction framework:

$$\underset{m}{\operatorname{argmin}} \frac{1}{2}\|DSm - y\|_2^2 + \lambda\|\Phi m\|_1 \quad (2)$$

Here, m is the desired image (3D spatial size: $N_x \times N_y \times N_z$), y is the acquired non-Cartesian data, S and D are defined in Equation [1] and Φ is the 3D Daubechies wavelet transform. The first term in Equation [2] is a data consistency term that minimizes the difference between the acquired data y and the reconstructed image m through the acquisition model. The second term enforces sparsity by minimizing the L1-norm of the wavelet coefficients of m, λ is the regularization parameter.

Soft-Gating L1-ESPIRiT Reconstruction

A common approach to correct for respiratory motion is gating, which selects a single motion state by rejecting data from the other states. This type of gating, which we refer to here as hard-gating, results in a relatively low scan efficiency. Alternatively, Johnson et al. (44), Cheng et al. (45) and also Forman et al. (46) proposed a simple and retrospective approach called soft-gating, in which all data is used but with weighting based on the estimated amount of respiratory motion. The concept of soft-gating is illustrated in the top branch of Figure 1. The weights effectively take account for motion induced data inconsistency. We use the soft-gating approach by modifying the basic image reconstruction model (Eq. [2]) to incorporate appropriate weights W:

$$\underset{m}{\operatorname{argmin}} \frac{1}{2}\|W(DSm - y)\|_2^2 + \lambda\|\Phi m\|_1 \quad (3)$$

Here, W is a diagonal matrix containing the soft-gating weights, which are applied to the data consistency term. Let $w[n]$ be the vector representing the diagonal entries of W. A different weight $w[n]$ is estimated for each radial spoke n, ranging between 0 and 1:

$$w[n] = \begin{cases} e^{\alpha(d[n] - \text{threshold})}, & \text{if } d[n] > \text{threshold} \\ 1, & \text{otherwise} \end{cases}, \quad (4)$$

where $d[n]$ represents the estimated respiratory motion with respect to the end of expiration or the end of inspiration (we picked the end of expiration state in this manuscript since more time is typically spent in expiration during a respiration cycle), *threshold* is a threshold of the respiratory motion, and α is a scaling factor. For data experiencing more respiratory motion corruption, their weights are smaller and thus they contribute less to the data consistency term in Equation [3].

Soft-gating parameters were experimentally tuned: a small set of parameters were tried and image quality was assessed visually to balance between motion blurring and SNR. We found that the weighting parameter α suggested by Zhang et al. (47) (3/max ($d[n]$)) provided good tradeoff, and hence was used for the rest of the study. The threshold parameter was set as 25% of the maximum respiratory position. We solved the optimization in Equation [3] using FISTA (61).

Respiratory Motion-Resolved L1-ESPIRiT Reconstruction

Another approach we propose to use for pulmonary imaging is a respiratory motion-resolved reconstruction. We take a similar approach as XD-GRASP proposed by Feng et al. (48): sorting the free-breathing data into an extra respiratory motion-states dimension and constraining sparsity along the motion-states dimension by compressed sensing. The respiratory motion-resolved approach modifies the basic image reconstruction model (Eq. [2]) by extending the desired image to be 4D (3D spatial + 1D motion-states), and enforces sparsity along the motion-states dimension:

$$\underset{M}{\operatorname{argmin}} \frac{1}{2}\|DSM - y\|_2^2 + \lambda_1\|\Phi M\|_1 + \lambda_2\|M\|_{TV} \quad (5)$$

Here, M is the desired respiratory motion-resolved images (3D spatial + 1D motion-states), y is the acquired non-Cartesian data reformatted into different motion states according to estimated respiration signal, S is the ESPIRiT sensitivity maps, and D is the non-Cartesian Fourier (3D Radial) operator in the first term that enforces data consistency. The second term enforces spatial sparsity by minimizing the L1-norm of the wavelet coefficients of M. The wavelet transform operator is represented by Φ. The third term enforces motion-state sparsity by minimizing the total variation (TV) norm along the extra respiratory motion dimension. λ_1 and λ_2 are the regularization weights for wavelet-domain sparsity and motion-state sparsity, respectively. We solved the optimization in Equation [3] using the alternating direction method of multipliers (ADMM) (63).

Imaging Studies and Data Processing

The proposed methods were applied on two healthy volunteers and nine clinical patients. All in vivo studies conducted were approved by our Institutional Review Board (IRB). Image

reconstruction and post-processing were carried out by the Berkeley Advanced Reconstruction Toolbox (BART) (64), including gridding and ESPIRiT calibration. In the spirit of reproducible research, we provide both MATLAB (MathWorks, Natick, MA) and Python (PSF, Wilmington, DE) demonstration code (https://github.com/jiangwenwen1231/FB_UTE_Recon) and a software package to reproduce some of the results described in this article. The software can be downloaded from: https://github.com/mrirecon/bart.

Experiments

All of the in vivo 3D UTE scans shared the following relevant parameters: prescribed field of view (FOV) = 32 × 32 × 32 cm^3, flip angle = 4°, 1.25 mm isotropic resolution, sampling bandwidth = ±250 kHz, readout duration = 1 ms. Gradients were designed to create a maximum shift of ±125 kHz across the prescribed FOV. The total scan time was between 5 min 7 s and 5 min 14 s, and between 75,800 and 109,800 spokes were acquired, which results in undersampling ratio ≈ 8 with respect to Nyquist criterion (π× Cartesian counterpart) when motion is ignored. TE was in the range of 70–80 μs and TR was in the range of 2.9–4.1 ms (TR varies with respect to the gradient hardware limits on different scanners).

Free-breathing scans were performed on all the subjects with slight different scan details: two healthy male volunteer (age 29 and 31) experiments were performed on 3T Discovery™ MR750 clinical scanners (GE Healthcare, Waukesha, WI) with an 8-channel cardiac coil and 20-channel torso coil arrays; eight clinical patients (including 6 CF patients) studies (4 males and 4 females, with age ranging from 11 to 72) were performed on 1.5T SIGNA™ HDx and 3T Discovery™ MR750w (GE Healthcare, Waukesha, WI) clinical scanners, an 8-channel cardiac coil and 18-channel torso coil were used as receiver arrays; the patient with pulmonary nodules (male, age 73) was scanned on a 3T SIGNA™ PET/MR scanner (GE Healthcare, Waukesha, WI) with a 18-channel torso coil. Respiration bellows belts were in place during all the scans.

Evaluation of Dynamic 3D Self-Navigator

For the dynamic 3D self-navigator, the beginning 16% of the data along the readout was used to reconstruct lower-resolution images and estimate sensitivity maps. This results in 7.5 mm apparent isotropic spatial resolution. Lower-resolution 3D self-navigators were reconstructed on a 80 × 80 × 80 matrix of each frame with a temporal window width of 100 spokes, which yields an apparent temporal resolution of ≈ 300 ms (depends on TR value). Effectively, every frame has the acceleration factor of 200 with respect to the Nyquist criterion. We partitioned the images with the block size of 8 × 8 × 8, and applied locally low-rank constraints on the temporal domain, using regularization of $\lambda = 0.0005$. For comparison, we performed a direct 3D gridding reconstruction on the same data of every temporal frame.

We compared dynamic 3D self-navigation with DC-based self-navigating and respiratory bellows navigation on a group of eight clinical patients with mixed patterns of breathing. Motion estimates from the dynamic 3D self-navigator were obtained by measuring the superior/inferior (SI) translation motion of the diaphragm by calculating cross correlations

on a region-of-interest (ROI) in image domain. For DC-based self-navigation, we applied a low-pass (0.5 Hz cut-off frequency) filter on the k-space center to extract the 1D respiration motion surrogate. An additional median filter was applied to the raw data. Finally, the asymmetric least-squares smoothing method (65) was performed to remove baseline drifts.

Pearson correlation coefficient analysis between different respiratory motion estimation methods for each subject was performed, in order to quantify the linear correlation between different respiratory motion signals. The motion estimation accuracy was further investigated by reconstructing images with the proposed soft-gating L1-ESPIRiT method. The soft-gating compensation used the same parameters across different motion estimations, including similar effective undersampling factors (which is defined by summing up the weighting values with respect to data size). The image quality was assessed by image sharpness along lung-liver interfaces with the maximum of the first derivative (MD) (27), normalized by the MD value of dynamic 3D self-navigator reconstructed images. A median filter was applied before taking the derivative to mitigate the noise sensitivity of the MD method. Ten slices were chosen to compute mean and standard deviation for each case.

Evaluation of Motion Compensated Reconstruction

Soft-gating L1-ESPIRiT was evaluated by first extracting the respiratory motion signals from the acquired data by the proposed 3D dynamic self-navigator ($80 \times 80 \times 80 \times 1000$ matrix). Then, we used 3D Daubechies wavelet basis with regularization values of $\lambda = 0.01$ in the soft-gating L1-ESPIRiT reconstruction. The results were compared with L1-ESPIRiT reconstruction without respiratory motion compensation.

For respiratory motion-resolved L1-ESPIRiT reconstruction algorithm, the same respiratory navigation signals were used. We divided the data equivalently into five motion states (each state has the same number of radial spokes). Regularization values of λ_1 and λ_2 were empirically selected with the qualitative criteria of suppressing aliasing artifacts and preventing blurring spatially/between motion states. More specifically, we set λ_2 to be zero and chose appropriate spatial sparsity weight λ_1 first. Then we add the motion-state weight λ_2 to improve the undersampling aliasing removal while keeping fidelity across motion states.

Feasibility for Cystic Fibrosis and Pulmonary Nodules

We also evaluated preliminary feasibility of the proposed methods in pathologies of CF and pulmonary nodules. The soft-gating L1-ESPIRiT reconstruction was implemented, with similar reconstruction parameters to those described above.

RESULTS

Evaluation of Dynamic 3D Self-Navigator

As seen in Figure 2, dynamic lower-resolution images have strong streaking artifacts when only the gridding operation was applied, due to a high level of undersampling (~ 200-fold) of every frame. It is extremely challenging to estimate motion information from these corrupted images. When parallel imaging and compressed sensing with LLR constraints

were applied, the aliasing artifacts were significantly reduced by the dynamic image sequence prior. The Supporting Video S1 shows the comparison of gridding and LLR images over time.

To demonstrate the dynamics captured by the dynamic 3D self-navigator, we selected cross lines perpendicular to the diaphragm, front chest wall, at the apex of the lung, in which complex breathing patterns were observed. In both case 1 and case 2 in Figure 2, the dynamic 3D navigators were capable of displaying the full chest motion pattern well, including lung–liver interface displacement, chest wall expanding, as well as movement of pulmonary vessels within the lung. Both subjects had a mixture of deep and shallow breathing patterns with variable rates. The Supporting Videos S2 and S3 clearly illustrate the full respiratory motion captured by the LLR reconstruction on two CF patients with complex breathing patterns.

Comparisons of the motion estimation signals and corresponding reconstructed images for two challenging clinical cases in which patients had mildly irregular breathing and strongly irregular breathing are shown in Figure 3, and quantitative comparisons across eight clinical cases are shown in Figure 4. The Supporting Video S4 shows the breathing pattern of the eight clinical patients evaluated in the Figure 4.

Case 1, shown in the left of Figure 3, had mildly irregular breathing, with periods of regular motion but also some deep/shallow inhalation. Both DC-based self-navigation and dynamic 3D navigator were able to delineate the deep and shallow inhalation (shaded areas at ≈ 30 s, 140 s) while the respiratory belt failed to capture this variation. The motion estimation accuracy was evaluated qualitatively by applying a soft-gating L1-ESPIRiT reconstruction, which is shown below the respiratory motion estimation plot in Figure 3. As the yellow arrows show, the sharpness of the small vessels was slightly deteriorated with respiratory belt navigation and DC-based self-navigation, while the dynamic 3D self-navigator most clearly depicts these fine structures and improves the conspicuity of the small vessels. Although the DC-based self-navigation motion estimation appeared to correctly capture deep and shallow inhalation and was strongly correlated with dynamic 3D navigator-based 1D motion estimation ($R = 0.8187$, Fig. 4), the blurred vessels in the reconstructed images indicate some inaccuracies. Both belt navigation and DC-based self-navigation resulted in lower average MD sharpness values at the lung-liver interface compared with 3D self-navigation (Fig. 4). The 3D self-navigator videos are included in the supplementary materials (Supporting Video S2).

Case 2, shown in the right of Figure 3, had a strongly irregular breathing pattern. Differences in the motion estimation results are largely due to the fact that respiratory belt and DC-based self-navigation cannot capture the bulk displacement of the lung and the diaphragm that occurred during this study. During several abrupt movements (shaded areas at ≈ 20 s, 70 s and 150 s), the respiration belt failed to match the actual displacement of diaphragm. We suspect this patient was coughing during the first minute of the scan. As the reconstructed images show below the respiratory motion estimation plot in Figure 3, images reconstructed utilizing DC-based self-navigation and respiratory belt had low vessel conspicuity and substantial blurring observed at the dome of the liver. This suggests both the DC and bellows

signals did not accurately represent chest wall and diaphragm motion. The dynamic 3D navigator gating clearly improves the image quality in this case, sharply recovering fine vascular structures within the lung. The significantly lower MD sharpness values from belt navigation and DC-based navigation of Case 2 in Figure 4 also support this result. In the supplementary materials, we provide the Supporting Video S3 showing the dynamic 3D navigator for this patient during the 5-min scan.

For the eight clinical patient studies, we compared the respiration estimation signals and the resulting image sharpness at the diaphragm from the dynamic 3D self-navigator, a DC-based self-navigator, and respiratory bellows belt-based navigation (Fig. 4). For the subjects with regular breathing patterns (Cases 4,7,8), respiratory bellow and DC-based self-navigation motion estimation signals had strong correlation with the dynamic 3D navigator based motion estimation (> 0.85). However, there was substantial disagreement for subjects with irregular breathing patterns (Cases 1,2,5,6) as indicated by lower correlation coefficients. Similar results across cases were observed in the diaphragm sharpness of soft-gating L1-ESPIRiT reconstructed images, as measured by the maximum derivative metric (27). For the subjects with regular breathing patterns (Cases 4,7,8), the different respiration estimation methods resulted in similar sharpness measures. For the subjects with irregular breathing patterns (Cases 1,2,5,6), using the dynamic 3D self-navigator for motion estimation had notably better sharpness measures than both DC-based self-navigation and respiratory bellow based images. In all our cases, using the dynamic 3D self-navigator for motion estimation provided equivalent or better image sharpness compared to respiratory bellows and DC-based self-navigation motion estimation.

(Respiratory motion dynamics of these eight clinical patients can be found in the Supporting Video S4).

Evaluation of Motion Compensated Image Reconstruction

Figure 5 shows a comparison of non-gated L1-ESPIRiT reconstruction (left) with our soft-gating L1-ESPIRiT reconstruction (right) in a healthy volunteer and a CF patient. The zoomed-in red boxes show that the fine pulmonary structures are delineated well with soft-gating L1-ESPIRiT. Red arrows point out where vessels and fine structures were blurred out by the respiratory motion when the non-gated reconstruction was used, while soft-gating L1-ESPIRiT was able to visualize the fine structures and diaphragm. Overall, soft-gating L1-ESPIRiT reconstruction also provides comparable apparent SNR, since it removes the both streaking and noise-like artifacts while enforcing sparsity in the image wavelet domain.

For motion-resolved reconstruction's selection of the two regularization parameters (λ_1 and λ_2), Figure 6 shows the results for six representative regularization combinations on the same volunteer in Figure 5. Both λ_1 of the wavelet sparsity and λ_2 of the motion states sparsity help to suppress undersampling aliasing artifacts. λ_1 promotes 3D spatial sparsity, effectively removing aliasing artifacts (shown in the top row of Fig. 6). Very high values of λ_1 introduce over-smoothing of images (the last figure in the first row). Usage of the additional sparsity constraint along the additional respiratory-state dimension improved the removal of undersampling artifacts (shown in the second row of Fig. 6). Not using motion states sparsity ($\lambda_2 = 0$) resulted in residual aliasing artifacts (the first figure in the second

row), while very high values of λ_2 introduced blurring over respiratory motion states (the last figure in the second row). Regularization values on the order of $\lambda_1 = 0.01$ and $\lambda_2 = 0.02$ were empirically tuned and used for reconstruction.

Figure 7 shows the respiratory motion-resolved images of all the respiratory motion-states (from left to right) from the same volunteer as Figure 5. They clearly depict respiratory motion without suffering from undersampling-induced aliasing. See the Supporting Video S5 for an animated version of the respiratory motion-resolved images.

Figure 8 shows a side-by-side comparison of the soft-gating and respiratory motion-resolved reconstructions on the same volunteer. Both soft-gating and respiratory motion-resolved techniques were able to significantly reduce motion blurring and artifacts due to undersampling. The two reconstructions have similar apparent image quality. While respiratory motion-resolved imaging provides all the motion states that could be valuable for dynamic evaluations (e.g., ventilation, air trapping), the soft-gating reconstruction is computationally more efficient. In this comparison carried out on a machine equipped with a four-socket Intel Xeon E7-8870 with a total of 144 cores at 2.10 GHz, our implementation of the motion-resolved L1-ESPIRiT reconstruction takes 156 GB memory and 5 h with our parallelized implementation, while soft-gating reconstruction takes 43 GB and 2 h on the same dataset.

To illustrate the performance of the motion compensated reconstructions in a subject with irregular breathing, Figure 9 shows a side-by-side comparison of the soft-gating and respiratory motion-resolved reconstructions for the CF patient Case 2 (also shown in Fig. 3). This subject had a strongly irregular breathing pattern and respiration drifts. Although the soft-gating technique was able to significantly reduce motion blurring and recover most of the vascular structures conspicuity within the lung, it resulted in blurring of some features (e.g., diaphragm and vessels, shown with yellow arrows). Due to the large variation of the respiratory motion and drifts, especially during inspiration state, we kept 60% of the data as shown in Figure 9 and then segmented the remaining data equally into five motion states to perform respiratory motion-resolved reconstruction. This respiratory motion-resolved reconstruction was able to delineate the small pulmonary vessels and sharp diaphragm, without deteriorating image quality. This is because each respiratory motion state represents smaller motion range compared with the soft-gating technique’s single motion state.

Feasibility for Cystic Fibrosis and Pulmonary Nodules

The top row of Figure 10 shows exemplary pathologies in CF that were well visualized when using the soft-gating L1-ESPIRiT reconstruction. The left case shows atelectasis along the major fissure (red arrow), and the middle and right cases show bronchiectasis. The middle case also shows mucus plugging, shown in the red circle. The air trapping is seen in the left lower lobe in the right case (red arrow). These demonstrate the potential of our approach to depict clinically relevant imaging features in the lung. Bottom row of Figure 10 shows clinical examples of a 3 mm, 5 mm, and 1 cm pulmonary nodules (green circles) when using the soft-gating L1-ESPIRiT reconstruction. The 3 mm nodule was an incidental finding from a volunteer study. This approach is able to depict a range of nodule sizes, shapes, and contrast as shown in these examples.

DISCUSSION

In this work, we present a motion robust method for high-resolution 3D pulmonary MRI. It is based on an optimized 3D UTE sequence and a free-breathing 5-min acquisition. The proposed methods include dynamic 3D images for self-navigation and motion estimation along with soft-gating L1-ESPIRiT and respiratory motion-resolved L1-ESPIRiT for robust motion compensated image reconstruction. With the proposed techniques, we have demonstrated that pulmonary structures are well delineated with good SNR, and overall improved image quality compared with traditional reconstructions.

Dynamic 3D Self-Navigator

The proposed lower-resolution dynamic 3D self-navigator utilizes locally low-rank constraints to reconstruct dynamic images from highly undersampled data. The resulting images can be used to robustly extract volumetric motion information of the entire chest. For patients with regular breathing patterns, we found that self-navigation based on DC signals provided similar gating quality compared with dynamic 3D navigator self-navigation. However, for patients with any irregular breathing or bulk motion, the dynamic 3D navigator was necessary to estimate the true motion. Being able to compensate for irregular breathing with the proposed method is critical for clinical pulmonary imaging applications, as these patients are more likely to have difficulty in breathing regularly.

Through comparing bellow-based, DC-based and dynamic 3D self-navigator based soft-gating reconstructions, we have shown that the accuracy of the 1D superior/inferior translation motion of the diaphragm affects the final image quality (Figs. 3 and 4). If the navigation signal results in inappropriate motion penalties for soft-gating reconstruction or incorrect motion bins for motion-resolved reconstruction, then the final image quality will degrade. We also compared motion-resolved reconstruction using DC-based motion estimation and dynamic 3D self-navigator for case 5, a CF patient, shown in Supporting Figure S1. In this patient, the Pearson correlation coefficient between DC and self-navigator is 0.4. Supporting Figure S1 shows representative images from three respiratory states—inspiration, transition, and expiration. In all of the motion states, many vessels are blurred out in DC-based reconstructed images, as indicated by the red arrows. Meanwhile, the diaphragm is sharper with 3D self-navigator based images as the yellow arrows show.

With the proposed lower-resolution dynamic 3D self-navigator, we have used it to estimate superior/inferior translation of the diaphragm. In our studies, the selection of particular location on the diaphragm did not make a noticeable difference as long as the diaphragm motion rhythm was spatially consistent. We believe the 3D navigator will allow for more detailed investigations into selection of this location and enhanced motion correction, but this is beyond the scope of the current work. In addition, there is abundant motion information that can be potentially utilized. With more comprehensive motion information, we could integrate the proposed 3D navigator with a more explicit motion compensation model. The lower-resolution dynamic 3D images itself may also provide additional diagnostic information about respiratory mechanics, including ventilation (66).

In addition, the proposed 3D navigator is not limited to 3D radial trajectory with bit-reversed pseudo-random ordering that was used in this study. It is easily translatable to other pseudo-random ordering schemes, like multi-dimensional golden angle ordering or other 3D trajectories, like 3D cones or radial-cones (42,67–69).

Soft-Gating versus Respiratory Motion-Resolved Method

The respiratory motion-resolved approach provides 4D results (3D spatial + motion-states), allowing comprehensive evaluations of pulmonary function such as ventilation and air trapping. Its primary limitation is that it is computationally expensive.

When relatively more time is spent in a single respiration motion state, as often occurs at end expiration, the soft-gating reconstruction is a practical choice to provide a high-quality image of that motion state, with reduced computational requirements. In some cases with irregular breathing patterns or drifts, motion blurring may still remain for soft-gating respiratory when the data below the threshold has experienced a large motion range. The motion-resolved reconstruction could provide improved results when each motion state data experiences less motion if they are carefully chosen. Both methods benefit from the quantitative and accurate estimation of the respiratory motion from the dynamic 3D self-navigator.

Several factors might contribute to the apparent SNR of the two reconstruction methods, such as the effective data sampling efficiency and regularization. The soft-gating sampling efficiency was about 40%, which is given by summing up the weighting values with respect to data size, and is higher than a single state data size of 20% in the respiratory motion-resolved method. The regularization parameters are also fundamentally different in the two reconstructions. Since the respiratory-motion resolved reconstruction has additional motion-state constraints, it is hard to make a fair comparison of SNR. However, the apparent SNR difference by subjective visual inspection between two reconstruction methods is not noticeable for the volunteer study in Figure 8.

One limitation of our proposed motion estimation method is that the overall process is not fully automated, as the identification of diaphragm was done manually. An accurate detection of the diaphragm could potentially be obtained using image segmentation. Furthermore, there is volumetric motion information beyond a single location in the diaphragm that can be potentially utilized. Further efforts are needed to minimize user interaction and leverage all motion information. Another limitation of the current implementation is that the reconstruction time is in the range of hours for both the dynamic 3D self-navigator and motion-resolved reconstructions on CPUs. We expect the computation time to be significantly reduced if our method is implemented on GPUs or clusters. For example, there is an upcoming distributed release of BART (64) with the potential for sub-second computations per iteration, which would be sufficient for clinical translation.

This work showed promising preliminary feasibility results of CF and pulmonary nodules, all within a 5-min scan time. Substantial clinical evaluations are still needed to verify the efficacy and robustness of the proposed method in these applications.

CONCLUSION

In this work, we have achieved motion robust high resolution 3D pulmonary imaging with MRI. We developed a method based on 5-min free-breathing scan using an optimized 3D radial UTE sequence and a dynamic 3D self-navigator for motion estimation, combined with state-of-the-art motion compensated reconstructions. This method was able to effectively eliminate motion artifacts even in the presence of strongly irregular breathing patterns, and reconstruct aliasing artifact-free images from highly undersampled data.

Supplementary Material

Refer to Web version on PubMed Central for supplementary material.

ACKNOWLEDGMENT

The authors would like to acknowledge Dr Joseph Cheng, Dr Tao Zhang, Dr Nicholas Burris and Dr Michael Hope for their helpful discussions.

Grant sponsor: NIH; Grant numbers: KL2TR000428, R01-EB019241, UL1TR000427; Grant sponsor: Sloan Research Fellowship from Sloan Foundation; Grant sponsor: Bakar Fellowship from UC-Berkeley; Grant sponsor: GEMS Fellowship from UCSF; Grant sponsor: Grant funding from General Electric Healthcare.

The authors receive research support from GE Healthcare.

REFERENCES

1. SmithBindman R, Miglioretti DL, Johnson E, et al. Use of diagnostic imaging studies and associated radiation exposure for patients enrolled in large integrated health care systems, 1996–2010. JAMA 2012;307:2400–2409. [PubMed: 22692172]
2. Bach PB, Mirkin JN, Oliver TK, et al. Benefits and harms of CT screening for lung cancer: a systematic review. JAMA 2012; 307: 2418–2429. [PubMed: 22610500]
3. Miglioretti DL, Johnson E, Williams A, et al. Pediatric computed tomography and associated radiation exposure and estimated cancer risk. JAMA Pediatr 2013;167:700–707. [PubMed: 23754213]
4. Kalra MK, Sodickson AD, MayoSmith WW. CT radiation: key concepts for gentle and wise use. RadioGraphics 2015;35:1706–1721. [PubMed: 26466180]
5. Bergin CJ, Pauly JM, Macovski A. Lung parenchyma: projection reconstruction MR imaging. Radiology 1991;179:777–781. [PubMed: 2027991]
6. Mayo JR, Mackay A, Müller NL. MR imaging of the lungs: value of short TE spin-echo pulse sequences. Am J Roentgenol 1992;159:951–956. [PubMed: 1414805]
7. Hatabu H, Gaa J, Tadamura E, Edinburgh KJ, Stock KW, Garpestad E, Edelman RR. MR imaging of pulmonary parenchyma with a half-fourier single-shot turbo spin-echo (HASTE) sequence. Eur J Radiol 1999;29:152–159. [PubMed: 10374663]
8. Ohno Y, Koyama H, Yoshikawa T, et al. N stage disease in patients with non–small cell lung cancer: efficacy of quantitative and qualitative assessment with STIR turbo spin-echo imaging, diffusion-weighted MR imaging, and fluorodeoxyglucose PET/CT. Radiology 2011;261:605–615. [PubMed: 21926377]
9. Lutterbey G, Gieseke J, Falkenhausen M, Morakkabati N, Schild H. Lung MRI at 3.0 T: a comparison of helical CT and high-field MRI in the detection of diffuse lung disease. Eur Radiol 2004;15:324–328. [PubMed: 15565313]
10. Weiger M, Hennel F, Pruessmann KP. Sweep MRI with algebraic reconstruction. Magn Reson Med 2010;64:1685–1695. [PubMed: 20949600]

11. Togao O, Tsuji R, Ohno Y, Dimitrov I, Takahashi M. Ultrashort echo time (UTE) MRI of the lung: assessment of tissue density in the lung parenchyma. Magn Reson Med 2010;64:1491–1498. [PubMed: 20574988]
12. Johnson KM, Fain SB, Schiebler ML, Nagle S. Optimized 3D ultra-short echo time pulmonary MRI. Magn Reson Med 2013;70:1241–1250. [PubMed: 23213020]
13. Burris NS, Johnson KM, Larson PEZ, Hope MD, Nagle SK, Behr SC, Hope TA. Detection of small pulmonary nodules with ultrashort echo time sequences in oncology patients by using a PET/MR system. Radiology 2016;278:239–246. [PubMed: 26133050]
14. Bannas P, Bell LC, Johnson KM, Schiebler ML, François CJ, Motosugi U, Consigny D, Reeder SB, Nagle SK. Pulmonary embolism detection with three-dimensional ultrashort echo time MR imaging: experimental study in canines. Radiology 2016;278:413–421. [PubMed: 26422185]
15. Brau ACS, Brittain JH. Generalized self-navigated motion detection technique: preliminary investigation in abdominal imaging. Magn Reson Med 2006;55:263–270. [PubMed: 16408272]
16. Larson AC, White RD, Laub G, McVeigh ER, Li D, Simonetti OP. Self-gated cardiac cine MRI. Magn Reson Med 2004;51:93–102. [PubMed: 14705049]
17. Crowe ME, Larson AC, Zhang Q, Carr J, White RD, Li D, Simonetti OP. Automated rectilinear self-gated cardiac cine Imaging. Magn Reson Med 2004;52:782–788. [PubMed: 15389958]
18. Buehrer M, Curcic J, Boesiger P, Kozerke S. Prospective self-gating for simultaneous compensation of cardiac and respiratory motion. Magn Reson Med 2008;60:683–690. [PubMed: 18727084]
19. Spincemaille P, Nguyen TD, Prince MR, Wang Y. Kalman filtering for real-time navigator processing. Magn Reson Med 2008;60:158–168. [PubMed: 18581354]
20. Bookwalter CA, Griswold MA, Duerk JL. Multiple overlapping k-space junctions for investigating translating objects (MOJITO). IEEE Trans Med Imaging 2010;29:339–349. [PubMed: 19709968]
21. Cheng JY, Alley MT, Cunningham CH, Vasanawala SS, Pauly JM, Lustig M. Nonrigid motion correction in 3D using autofocusing with localized linear translations. Magn Reson Med 2012;68:1785–1797. [PubMed: 22307933]
22. Manka R, Buehrer M, Boesiger P, Fleck E, Kozerke S. Performance of simultaneous cardiac-respiratory self-gated three-dimensional MR imaging of the heart: initial experience. Radiology 2010;255:909–916. [PubMed: 20501728]
23. Weick S, Breuer FA, Ehses P, Völker M, Hintze C, Biederer J, Jakob PM. DC-gated high resolution three-dimensional lung imaging during free-breathing. J Magn Reson Imaging 2013;37:727–732. [PubMed: 22987283]
24. Usman M, Vaillant G, Atkinson D, Schaeffter T, Prieto C. Compressive manifold learning: estimating one-dimensional respiratory motion directly from undersampled K-space data. Magn Reson Med 2014;72:1130–1140. [PubMed: 24357143]
25. Higano NS, Hahn AD, Tkach JA, Cao X, Walkup LL, Thomen RP, Merhar SL, Kingma PS, Fain SB, Woods JC. Retrospective respiratory self-gating and removal of bulk motion in pulmonary UTE MRI of neonates and adults. Magn Reson Med 2016;77:1284–1295. [PubMed: 26972576]
26. Paul J, Divkovic E, Wundrak S, Bernhardt P, Rottbauer W, Neumann H, Rasche V. High-resolution respiratory self-gated golden angle cardiac MRI: comparison of self-gating methods in combination with k-t SPARSE SENSE. Magn Reson Med 2015;73:292–298. [PubMed: 24478142]
27. Tibiletti M, Paul J, Bianchi A, Wundrak S, Rottbauer W, Stiller D, Rasche V. Multistage three-dimensional UTE lung imaging by image-based self-gating. Magn Reson Med 2016;75:1324–1332. [PubMed: 25940111]
28. Batchelor PG, Atkinson D, Irarrazaval P, Hill DLG, Hajnal J, Larkman D. Matrix description of general motion correction applied to multi-shot images. Magn Reson Med 2005;54:1273–1280. [PubMed: 16155887]
29. Odille F, Vuissoz PA, Marie PY, Felblinger J. Generalized reconstruction by inversion of coupled systems (GRICS) applied to free-breathing MRI. Magn Reson Med 2008;60:146–157. [PubMed: 18581355]
30. Cruz G, Atkinson D, Buerger C, Schaeffter T, Prieto C. Accelerated motion corrected three-dimensional abdominal MRI using total variation regularized SENSE Reconstruction. Magn Reson Med 2016;75: 1484–1498. [PubMed: 25996443]

31. Manke D, Rosch P, Nehrke K, Bornert P, Dossel O. Model evaluation and calibration for prospective respiratory motion correction in coronary MR angiography based on 3-D image registration. IEEE Trans Med Imaging 2002;21:1132–1141. [PubMed: 12564881]
32. Kellman P, Chefd'hotel C, Lorenz CH, Mancini C, Arai AE, McVeigh ER. High spatial and temporal resolution cardiac cine MRI from retrospective reconstruction of data acquired in real time using motion correction and resorting. Magn Reson Med 2009;62:1557–1564. [PubMed: 19780155]
33. Bhat H, Ge L, NiellesVallespin S, Zuehlsdorff S, Li D. 3D radial sampling and 3D affine transform-based respiratory motion correction technique for free-breathing whole-heart coronary MRA with 100% imaging efficiency. Magn Reson Med 2011;65:1269–1277. [PubMed: 21500255]
34. Xue H, Ding Y, Guetter C, Jolly MP, Guehring J, Zuehlsdorff S, Simonetti OP. Motion compensated magnetic resonance reconstruction using inverse-consistent deformable registration: application to real-time cine imaging. Med Image Comput Comput Assist Interv 2011;14:564–572. [PubMed: 22003663]
35. Schmidt JFM, Buehrer M, Boesiger P, Kozerke S. Nonrigid retrospective respiratory motion correction in whole-heart coronary MRA. Magn Reson Med 2011;66:1541–1549. [PubMed: 21604297]
36. Buerger C, Prieto C, Schaeffter T. Highly efficient 3D motion-compensated abdomen MRI from undersampled golden-RPE acquisitions. Magn Reson Mater Phys Biol Med 2013;26:419–429.
37. Asif MS, Hamilton L, Brummer M, Romberg J. Motion-adaptive spatio-temporal regularization for accelerated dynamic MRI. Magn Reson Med 2013;70:800–812. [PubMed: 23132400]
38. Paschke NK, Dössel O, Schaeffter T, Prieto C, Kolbitsch C. Comparison of image-based and reconstruction-based respiratory motion correction for golden radial phase encoding coronary MR angiography. J Magn Reson Imaging 2015;42:964–971. [PubMed: 25639861]
39. Rank CM, Heußer T, Buzan MTA, Wetscherek A, Freitag MT, Dinkel J, Kachelrieß M. 4D respiratory motion-compensated image reconstruction of free-breathing radial MR data with very high undersampling. Magn Reson Med 2016;77:1170–1183. [PubMed: 26991911]
40. Loktyushin A, Nickisch H, Pohmann R, Schölkopf B. Blind retrospective motion correction of MR images. Magn Reson Med 2013;70: 1608–1618. [PubMed: 23401078]
41. Moghari MH, Roujol S, Chan RH, et al. Free-breathing 3D cardiac MRI using iterative image-based respiratory motion correction. Magn Reson Med 2013;70:1005–1015. [PubMed: 23132549]
42. Ingle RR, Wu HH, Addy NO, Cheng JY, Yang PC, Hu BS, Nishimura DG. Nonrigid autofocus motion correction for coronary MR angiography with a 3D cones trajectory. Magn Reson Med 2014;72:347–361. [PubMed: 24006292]
43. Luo J, Addy NO, Ingle RR, Baron CA, Cheng JY, Hu BS, Nishimura DG. Nonrigid motion correction with 3D image-based navigators for coronary MR angiography. Magn Reson Med 2016;77:1884–1893. [PubMed: 27174673]
44. Johnson KM, Block WF, Reeder SB, Samsonov A. Improved least squares MR image reconstruction using estimates of K-space data consistency. Magn Reson Med 2012;67:1600–1608. [PubMed: 22135155]
45. Cheng JY, Zhang T, Ruangwattanapaisarn N, Alley MT, Uecker M, Pauly JM, Lustig M, Vasanawala SS. Free-breathing pediatric MRI with nonrigid motion correction and acceleration. J Magn Reson Imaging 2015;42:407–420. [PubMed: 25329325]
46. Forman C, Piccini D, Grimm R, Hutter J, Hornegger J, Zenge MO. Reduction of respiratory motion artifacts for free-breathing whole-heart coronary MRA by weighted iterative reconstruction. Magn Reson Med 2015;73:1885–1895. [PubMed: 24912763]
47. Zhang T, Cheng JY, Potnick AG, Barth RA, Alley MT, Uecker M, Lustig M, Pauly JM, Vasanawala SS. Fast pediatric 3D free-breathing abdominal dynamic contrast enhanced MRI with high spatiotemporal resolution. J Magn Reson Imaging 2015;41:460–473. [PubMed: 24375859]
48. Feng L, Axel L, Chandarana H, Block KT, Sodickson DK, Otazo R. XD-GRASP: golden-angle radial MRI with reconstruction of extra motion-state dimensions using compressed sensing. Magn Reson Med 2016;75:775–788. [PubMed: 25809847]
49. Pruessmann KP, Weiger M, Börnert P, Boesiger P. Advances in sensitivity encoding with arbitrary K-space trajectories. Magn Reson Med 2001;46:638–651. [PubMed: 11590639]

50. Lustig M, Donoho D, Pauly JM. Sparse MRI: the application of compressed sensing for rapid MR imaging. Magn Reson Med 2007;58: 1182–1195. [PubMed: 17969013]
51. Trzasko J, Manduca A, Borisch E. Local versus global low-rank promotion in dynamic MRI series reconstruction. In Proceedings of ISMRM, Montreél, Canada, 2011, p. 4371.
52. Zhang T, Pauly JM, Levesque IR. Accelerating parameter mapping with a locally low rank constraint. Magn Reson Med 2015;73:655–661. [PubMed: 24500817]
53. Uecker M, Lai P, Murphy MJ, Virtue P, Elad M, Pauly JM, Vasanawala SS, Lustig M. ESPIRiT—an Eigenvalue approach to auto-calibrating parallel MRI: where SENSE meets GRAPPA. Magn Reson Med 2014;71:990–1001. [PubMed: 23649942]
54. Gibiino F, Sacolick L, Menini A, Landini L, Wiesinger F. Free-breathing, zero-TE MR lung imaging. MAGMA 2015;28:207–215. [PubMed: 25200814]
55. Zhang T, Cheng JY, Chen Y, Nishimura DG, Pauly JM, Vasanawala SS. Robust self-navigated body MRI using dense coil arrays. Magn Reson Med 2016;76:197–205. [PubMed: 26220204]
56. Liu J, Drangova M. Combination of multidimensional navigator echoes data from multielement RF coil. Magn Reson Med 2010;64:1208–1214. [PubMed: 20564594]
57. Feng L, Axel L, Latson LA, Xu J, Sodickson DK, Otazo R. Compressed sensing with synchronized cardio-respiratory sparsity for free-breathing cine MRI: initial comparative study on patients with arrhythmias. J Cardiovasc Magn Reson 2014;16:1–2. [PubMed: 24387349]
58. Liu J, Spincemaille P, Codella NCF, Nguyen TD, Prince MR, Wang Y. Respiratory and cardiac self-gated free-breathing cardiac CINE imaging with multiecho 3D hybrid radial SSFP acquisition. Magn Reson Med 2010;63:1230–1237. [PubMed: 20432294]
59. Benner T, van der Kouwe AJ, Kirsch JE, Sorensen AG. Real-time RF pulse adjustment for b0 drift correction. Magn Reson Med 2006;56: 204–209. [PubMed: 16767763]
60. Vos SB, Tax CMW, Luijten PR, Ourselin S, Leemans A, Froeling M. The importance of correcting for signal drift in diffusion MRI. Magn Reson Med 2017;77:285–299. [PubMed: 26822700]
61. Beck A, Teboulle M. A fast iterative shrinkage-thresholding algorithm for linear inverse problems. SIAM J Imaging Sci 2009;2:183–202.
62. Figueiredo MAT, Nowak RD. An EM algorithm for wavelet-based image restoration. IEEE Trans Image Process 2003;12:906–916. [PubMed: 18237964]
63. Boyd S, Parikh N, Chu E, Peleato B, Eckstein J. Distributed optimization and statistical learning via the alternating direction method of multipliers. Found Trends Mach Learn 2011;3:1–122.
64. Uecker M, Tamir JI, Ong F, Iyer S, Cheng JY, Lustig M. BART: Berkeley Advanced Reconstruction Toolbox. In Proceedings of the Annual meeting ISMRM, Toronto, Canada, 2015. doi:10.5281/zenodo.50726.
65. Peng J, Peng S, Jiang A, Wei J, Li C, Tan J. Asymmetric least squares for multiple spectra daseline correction. Anal Chim Acta 2010;683: 63–68. [PubMed: 21094382]
66. Bhave S, Lingala SG, Newell JD, Nagle SK, Jacob M. Blind compressed sensing enables 3-dimensional dynamic free breathing magnetic resonance imaging of lung volumes and diaphragm motion Investigative Radiology. 2016;51:387–399. [PubMed: 26863578]
67. Addy NO, Ingle RR, Wu HH, Hu BS, Nishimura DG. High-resolution variable-density 3D cones coronary MRA. Magn Reson Med 2015;74: 614–621. [PubMed: 26172829]
68. Addy NO, Ingle RR, Luo J, Baron CA, Yang PC, Hu BS, Nishimura DG. 3D image-based navigators for coronary MR angiography. Magn Reson Med 2016;77:1874–1883. [PubMed: 27174590]
69. Johnson KM. Hybrid radial-cones trajectory for accelerated MRI. Magn Reson Med 2016;77:1068–1081. [PubMed: 27017991]

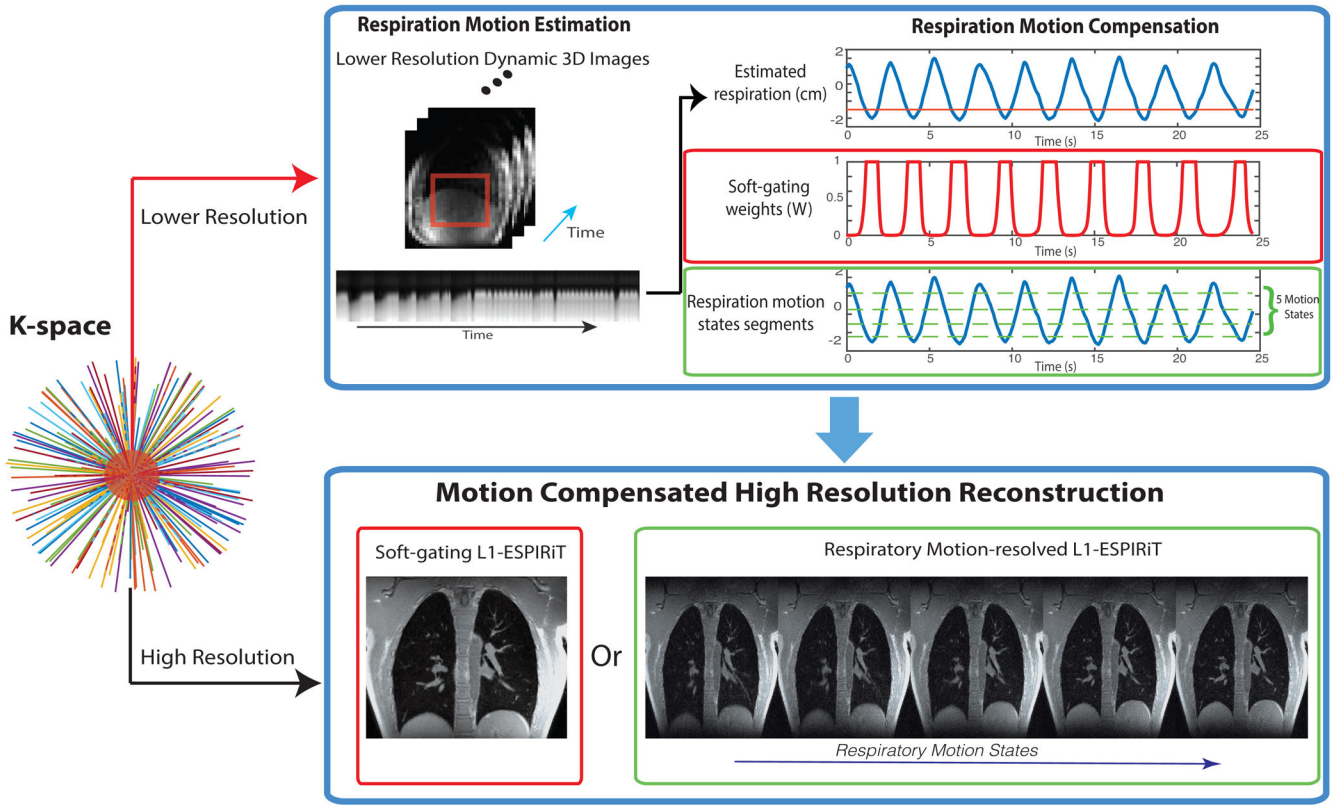

FIG. 1.

Illustration of the proposed methods: (*top branch*) Respiratory motion estimation from a dynamic 3D self-navigator, reconstructed using a central k-space region. This estimation is used to derive motion compensation information for the soft-gating and motion-resolved methods. The red line in the top respiration signal plot illustrates the soft-gating threshold. (*bottom branch*) Respiratory motion compensated reconstruction of high resolution images based on soft-gating and respiratory motion-resolved methods using the 1D motion surrogate signal derived from top branch.

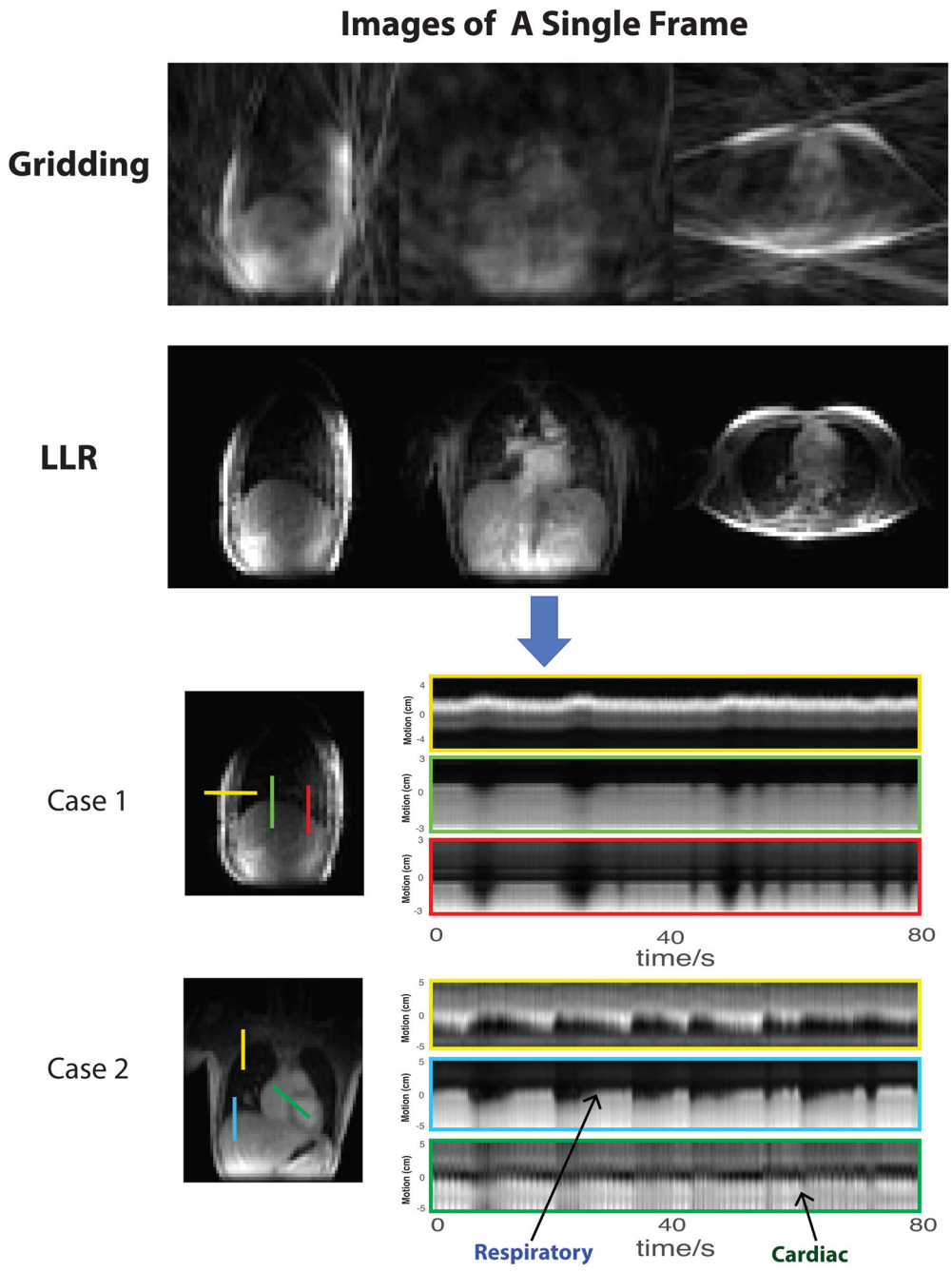

FIG. 2.

Dynamic 3D self-navigator: (top) Comparison of gridding and locally low-rank constrained lower-resolution images as navigators (Please see Supporting Video S1); (bottom) Motion measured by the LLR dynamic 3D self-navigator for two subjects with CF in which complex breathing patterns were observed. The cross lines of particular positions over time show multiple directions of chest motion. (Please see Supporting Videos S2 and S3 of these two cases.).

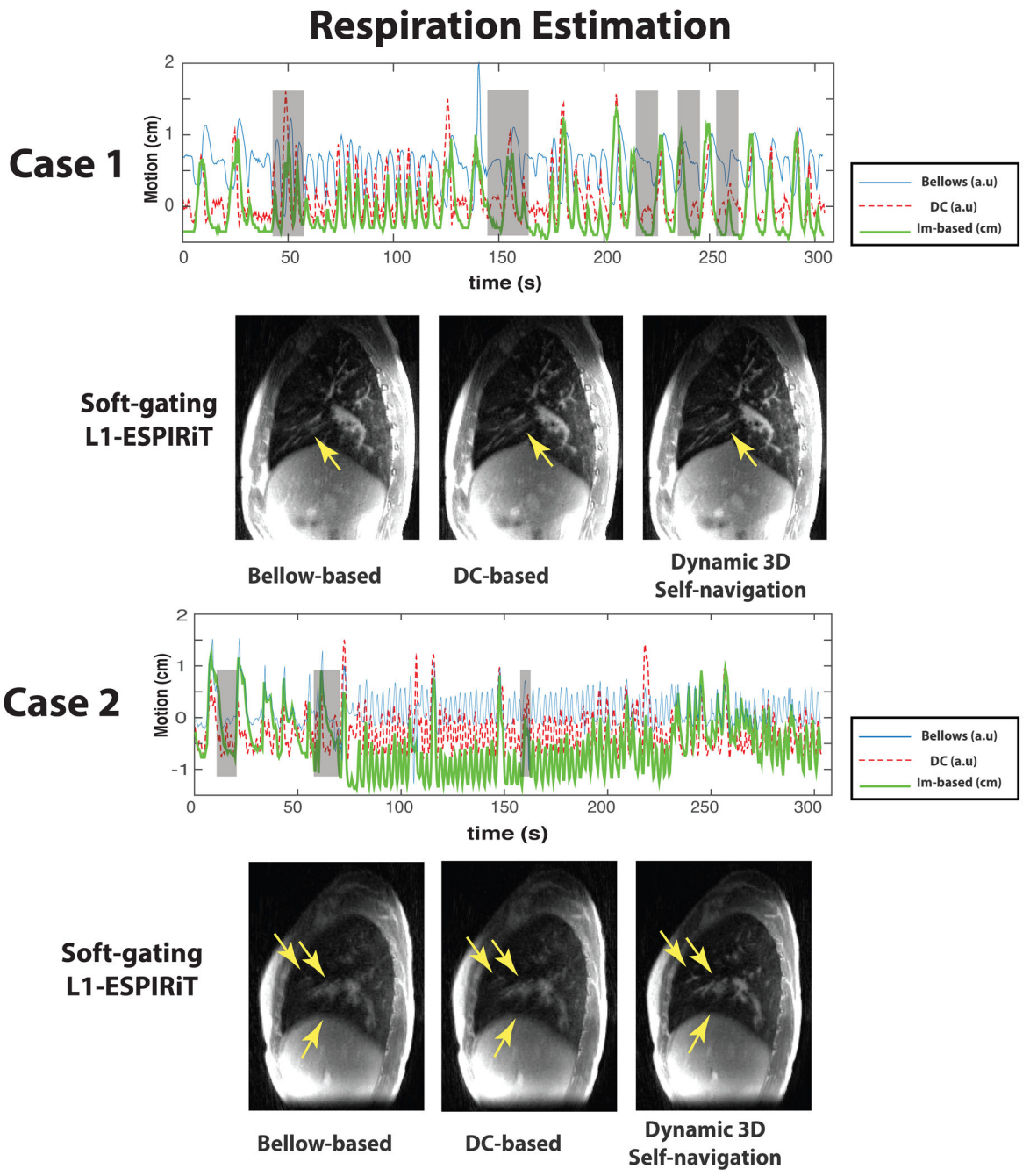

FIG. 3.

Comparison of different respiration estimation methods in CF patient case 1 with a mildly irregular breathing pattern and CF patient case 2 with a strongly irregular breathing pattern: In plots, (blue) respiration motion estimated by the respiratory bellows belt (“bellows”); (red dashed) respiration motion derived from the center of k-space (“DC”); (green) respiration SI motion derived from the dynamic 3D navigator (“Im-based”). Note that the only dynamic 3D self-navigation signal is quantitative (units of cm) whereas the DC-based and bellows are only relative measurements. Gray shaded boxes highlighted the time points where bellow signal/DC-based self-navigation differ a lot with dynamic 3D navigator. Comparisons of

soft-gating L1-ESPIRiT reconstructions based on corresponding respiration estimations are shown below the plots. These reconstructions are based on a soft weighting window centered at the end of expiration. The arrows indicate vessels with varying conspicuity based on different respiration estimations.

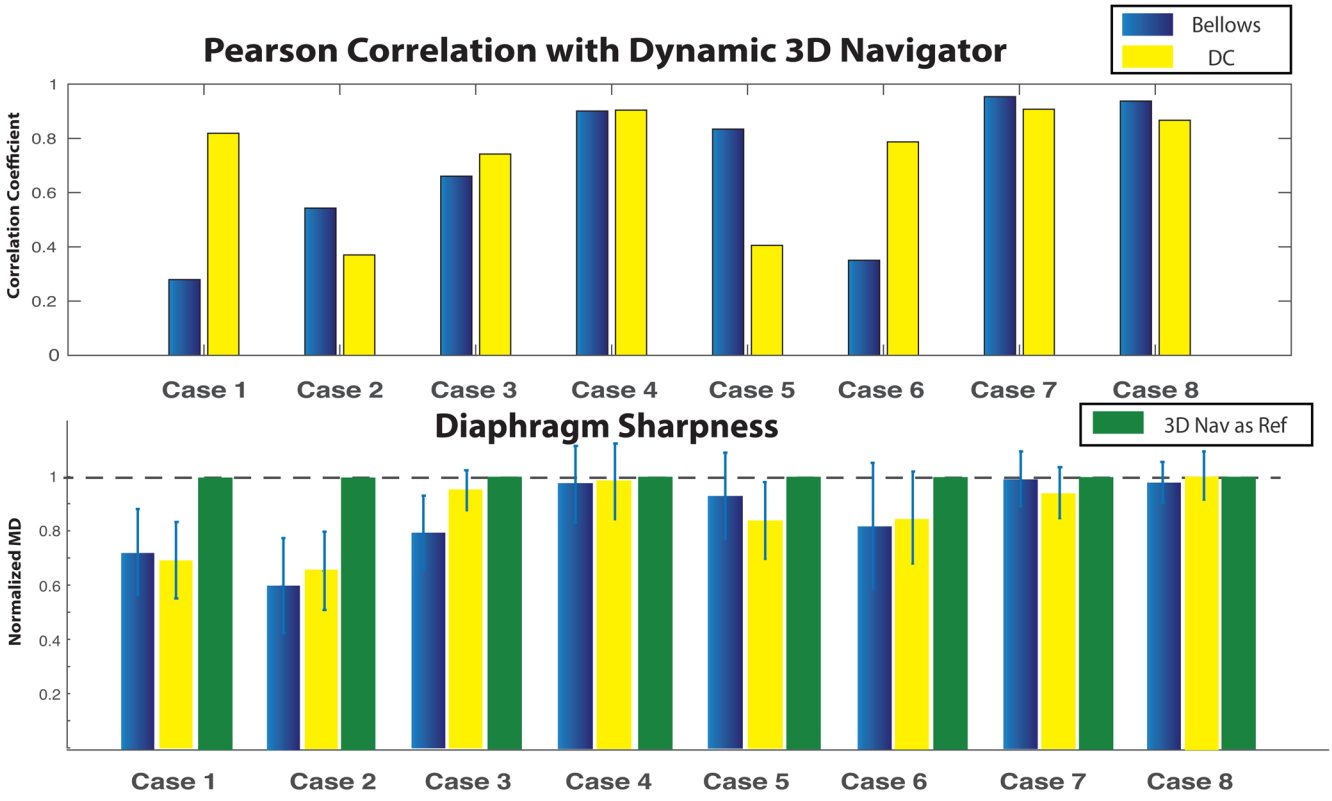

FIG. 4.

Quantitative comparison of respiration estimation methods among eight clinical patients: (Top) Pearson correlation coefficients between the dynamic 3D self-navigator signal and respiratory bellow signal (blue), and between dynamic 3D self-navigator signal and DC-based self-navigation signal (yellow); (Bottom) Comparison of diaphragm sharpness by the maximum derivative (MD) method. The MD values are normalized by the sharpness value of the dynamic 3D self-navigator reconstruction (reference MD value = 1).

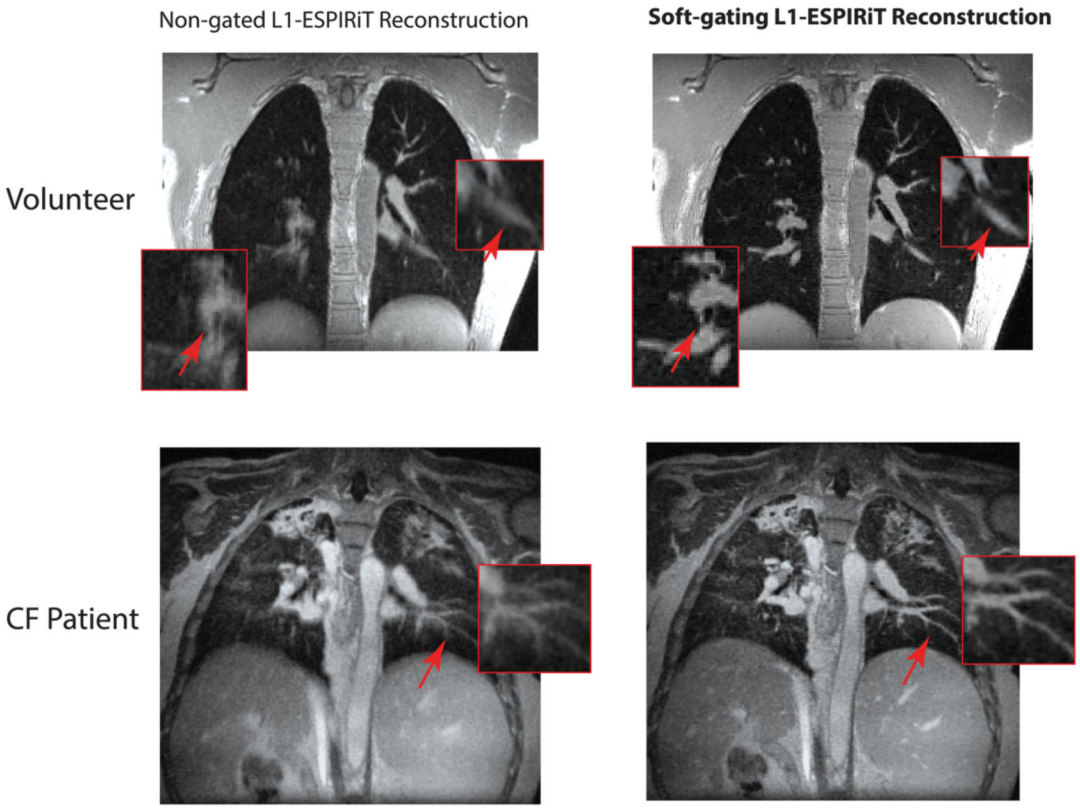

FIG. 5.

Comparison of soft-gating L1-ESPIRiT reconstruction with non-gated L1-ESPIRiT reconstruction showing a single coronal slice from a healthy volunteer (top row) and a cystic fibrosis patient (bottom row). Red boxes are zoomed-in views of fine structures, and arrows point out where vessels and fine structures were blurred out by the respiratory motion when the non-gated L1-ESPIRiT reconstruction was used, while soft-gating L1-ESPIRiT was able to visualize the fine structures and diaphragm.

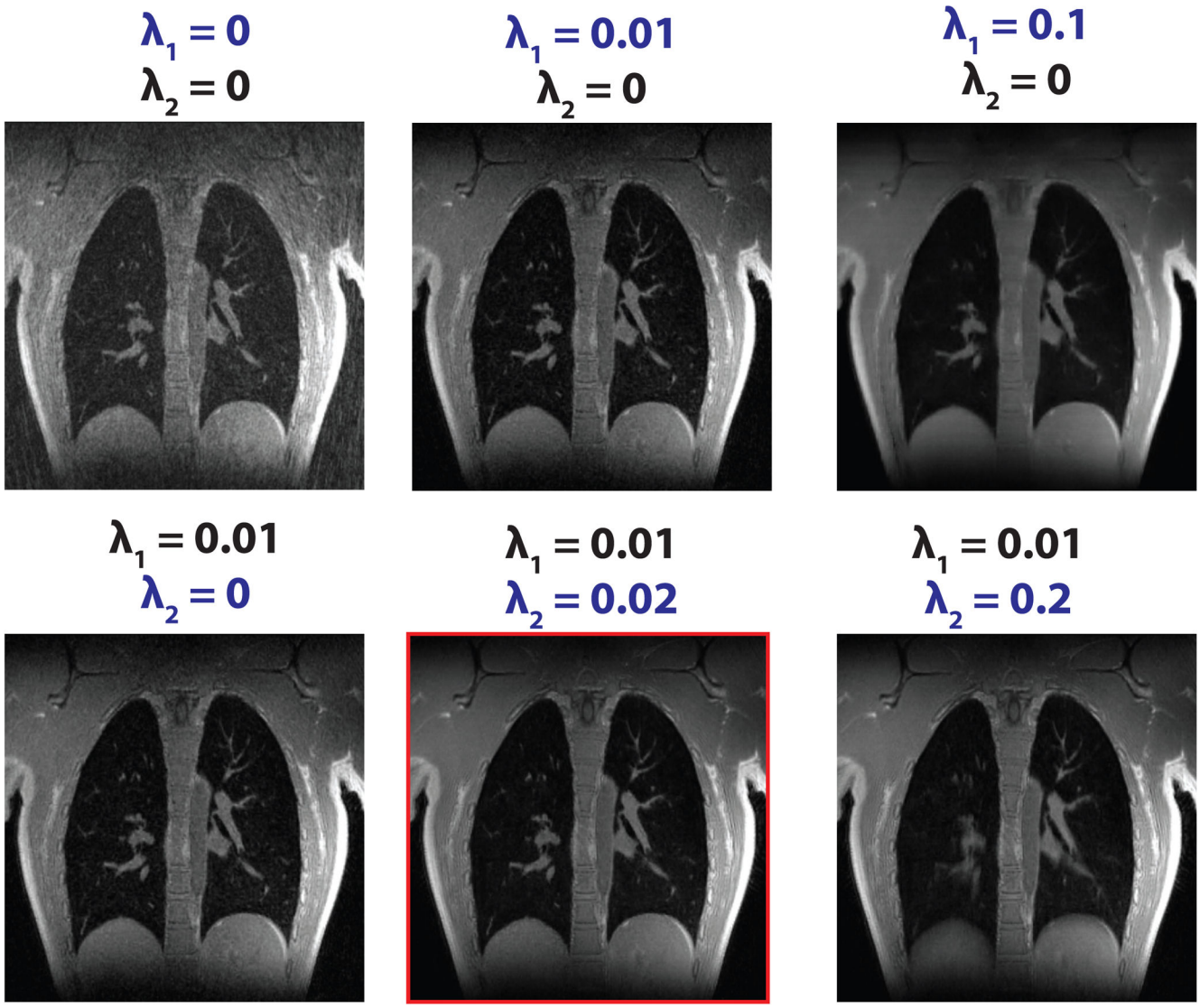

FIG. 6.

Respiratory motion-resolved reconstruction results for representative regularization parameters combinations on a healthy volunteer. λ_1 (wavelet sparsity) promotes 3D spatial sparsity, effectively removing many aliasing artifacts (shown in the top row). Usage of additional sparsity constraint along the additional respiratory-state dimension (λ_2) improved the removal of undersampling artifacts (shown in the second row). Very high values of λ_1 introduce over-smoothing of images (last figure in the first row), while very high values of λ_2 introduce blurring over respiratory motion states (last figure in the second row).

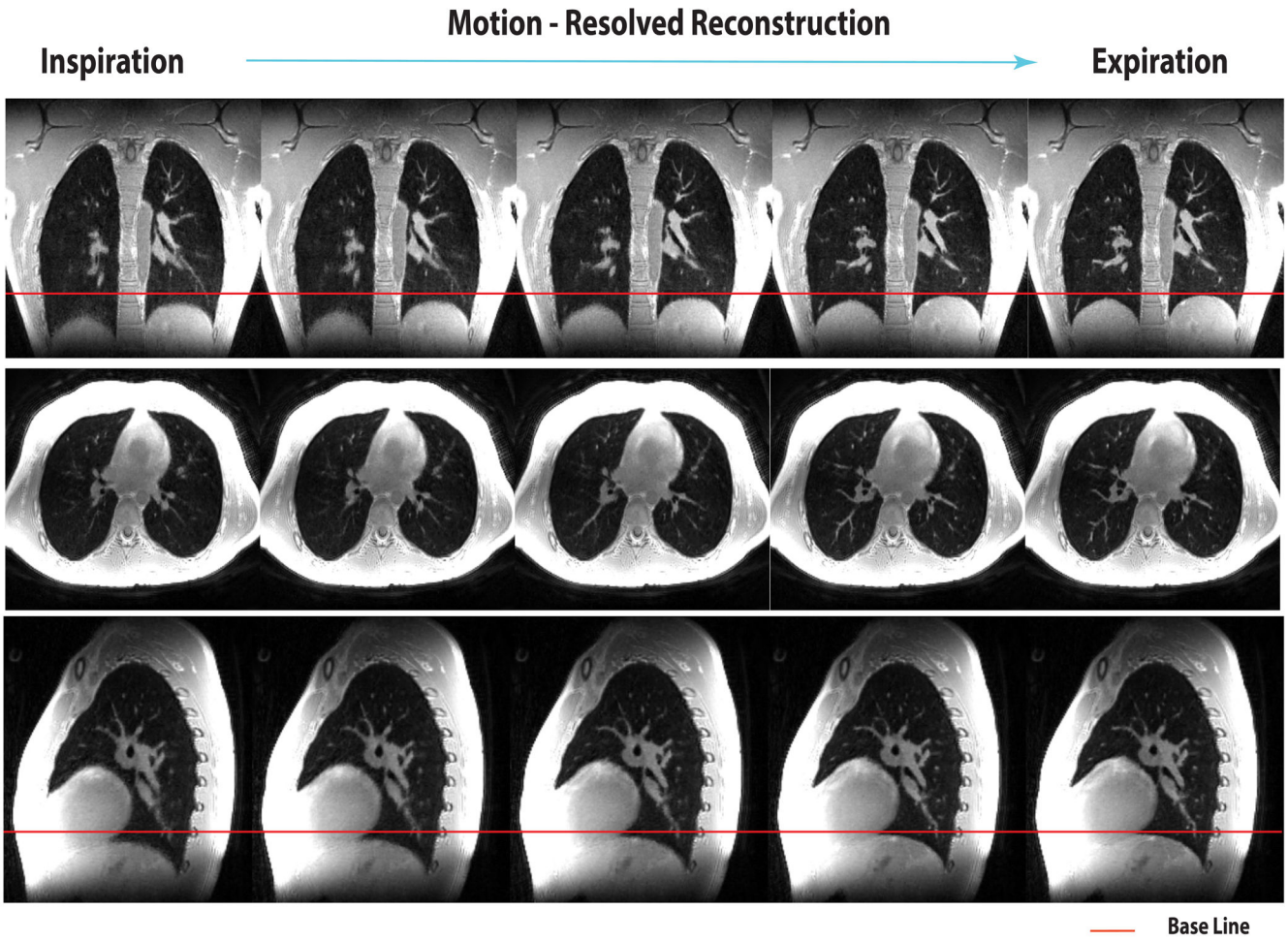

FIG. 7.

Respiratory motion-resolved L1-ESPIRiT reconstruction (images of different motion states are displayed from left to right). Please see the Supporting Video S5 for animated version of this result. The red line denotes the location of the diaphragm at end expiration.

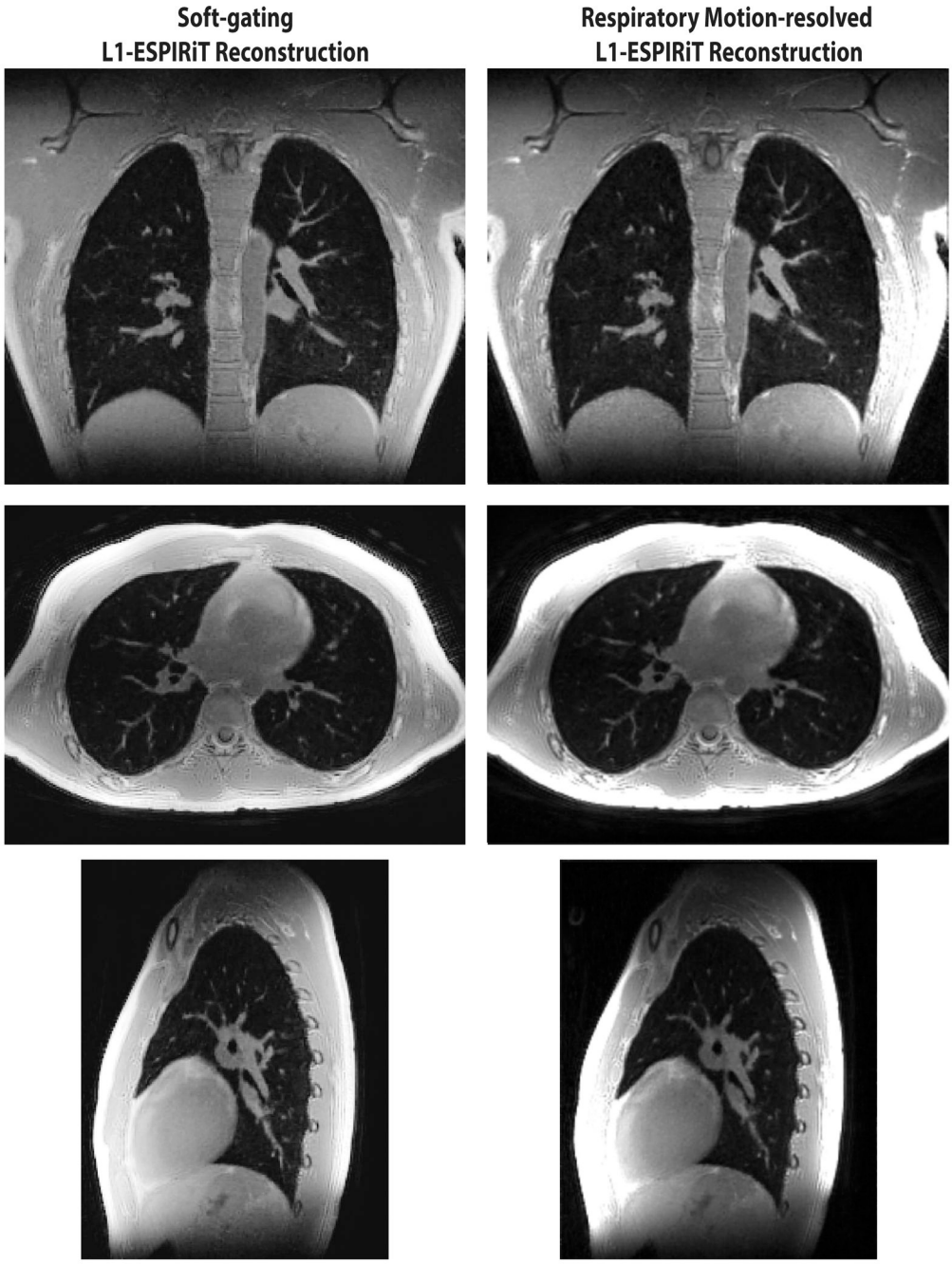

FIG. 8.

Comparison of soft-gating and respiratory motion-resolved L1-ESPIRiT reconstructions at end-expiration in a healthy volunteer.

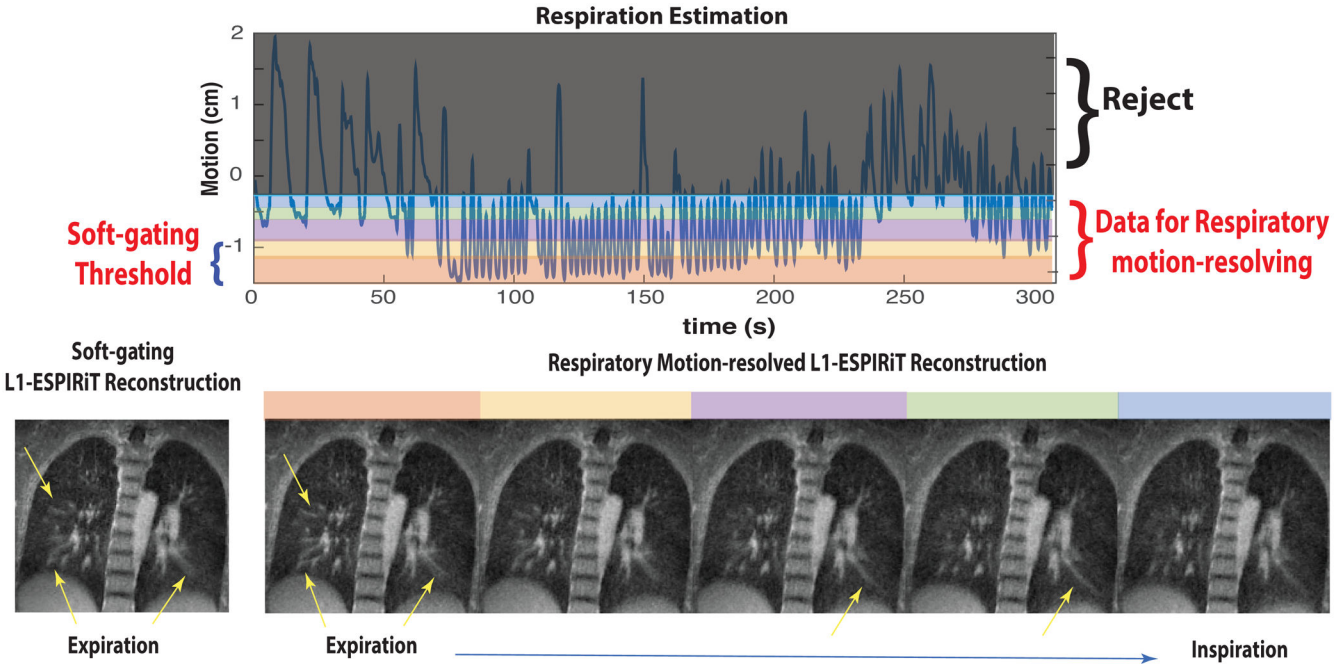

FIG. 9.

Comparison of soft-gating L1-ESPIRiT at end-expiration and respiratory motion-resolved L1-ESPIRiT reconstruction in a CF patient with strongly irregular breathing and respiration drifts (also shown in Fig 3 and Supporting Video S3). Due to the large variation of the respiratory motion and drifts, we kept 60% of the data as shown above and then performed respiratory motion-resolved L1-ESPIRiT reconstruction on the remaining data. Yellow arrows point out the features that still suffered from blurring artifacts with soft-gating, while the respiratory motion-resolved method was able to delineate the small pulmonary vessels and provide a sharp diaphragm.

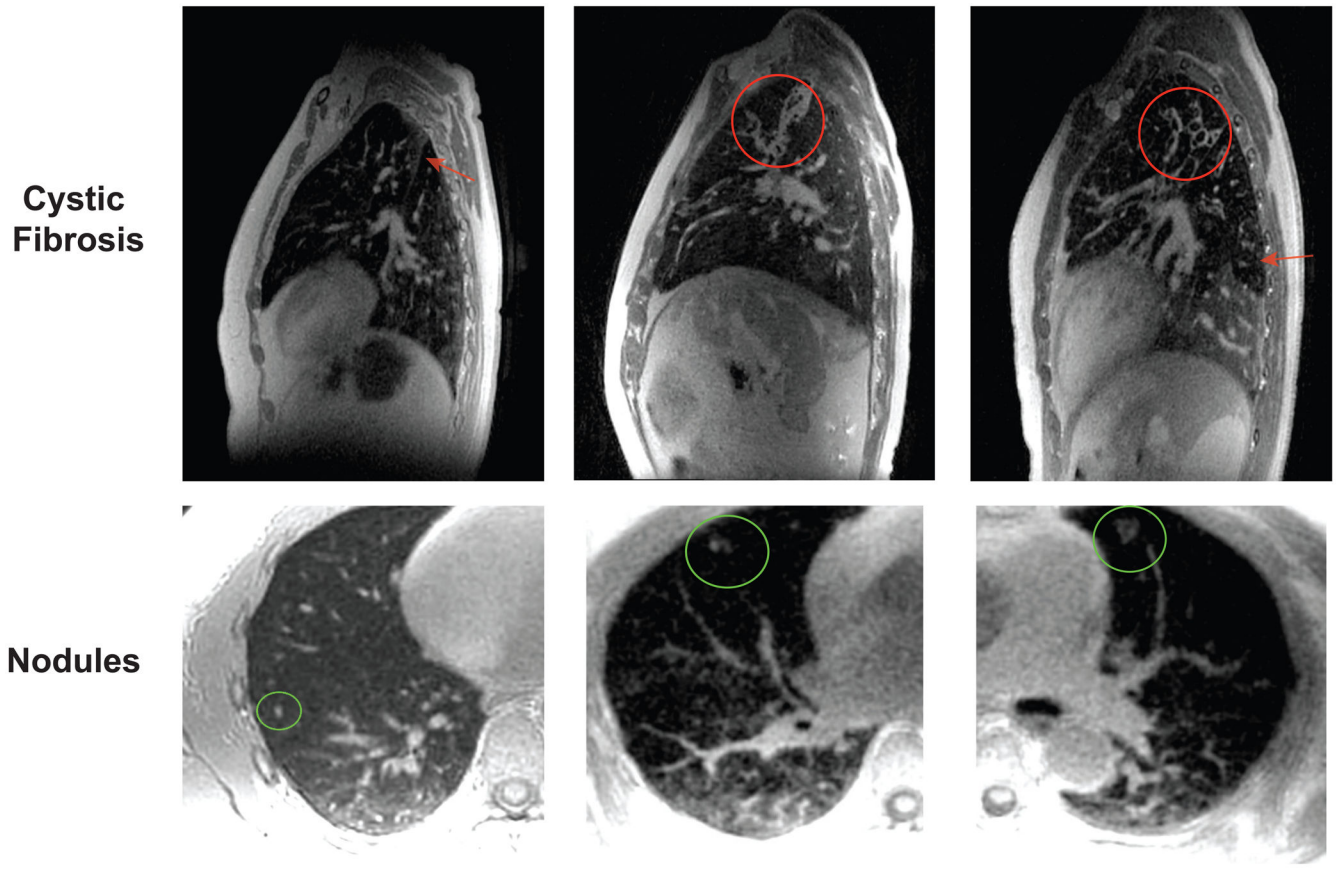

FIG. 10.

Top: soft-gating L1-ESPIRiT reconstruction in cystic fibrosis patients at end expiration: atelectasis (in the left case) along the major fissure, bronchiectasis and mucus plugging (in the middle case), bronchiectasis and air trapping (in the right case). Bottom: soft-gating L1-ESPIRiT reconstruction showing 3 mm, 5 mm, and 1 cm pulmonary nodules in different subjects.